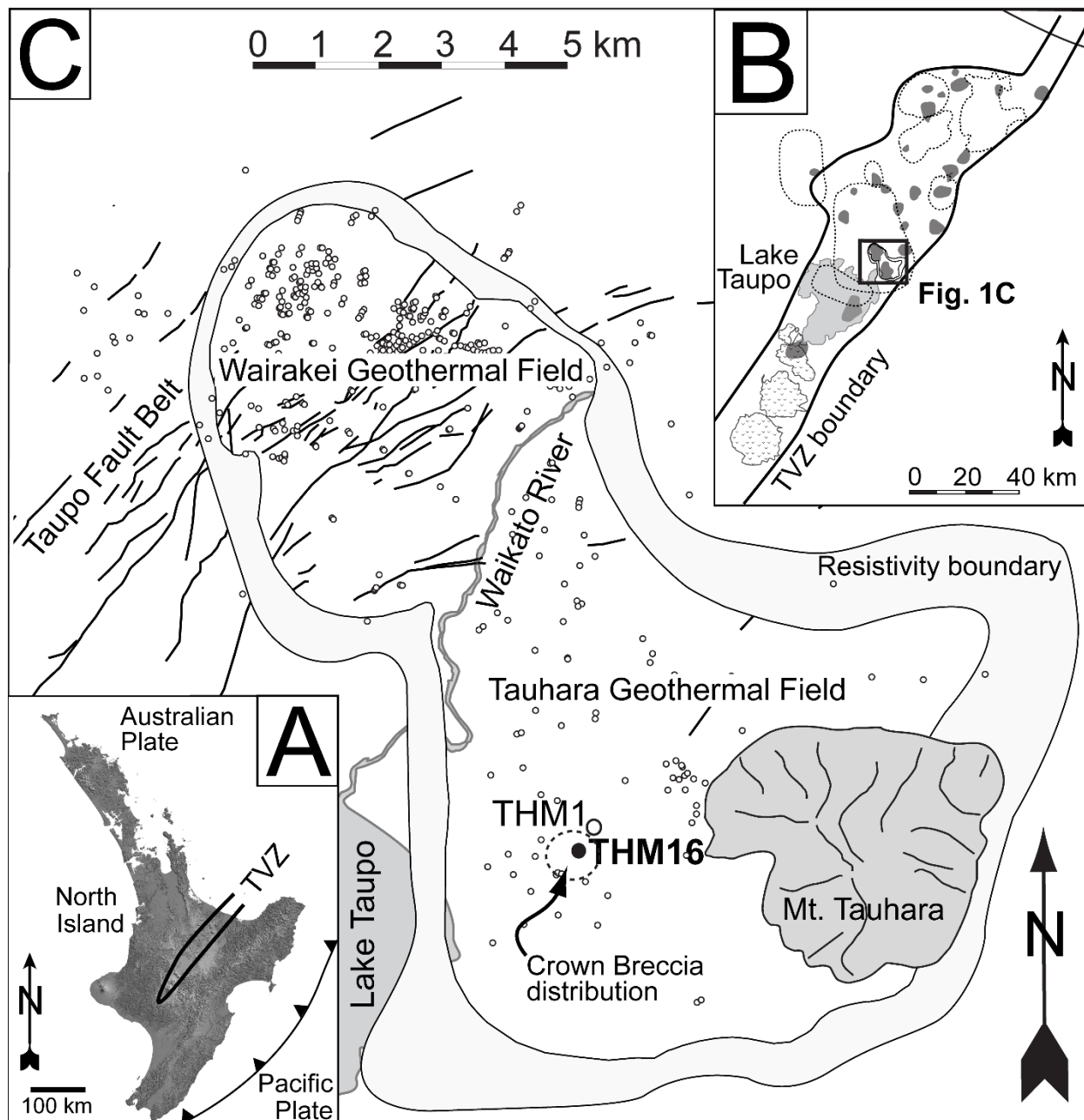
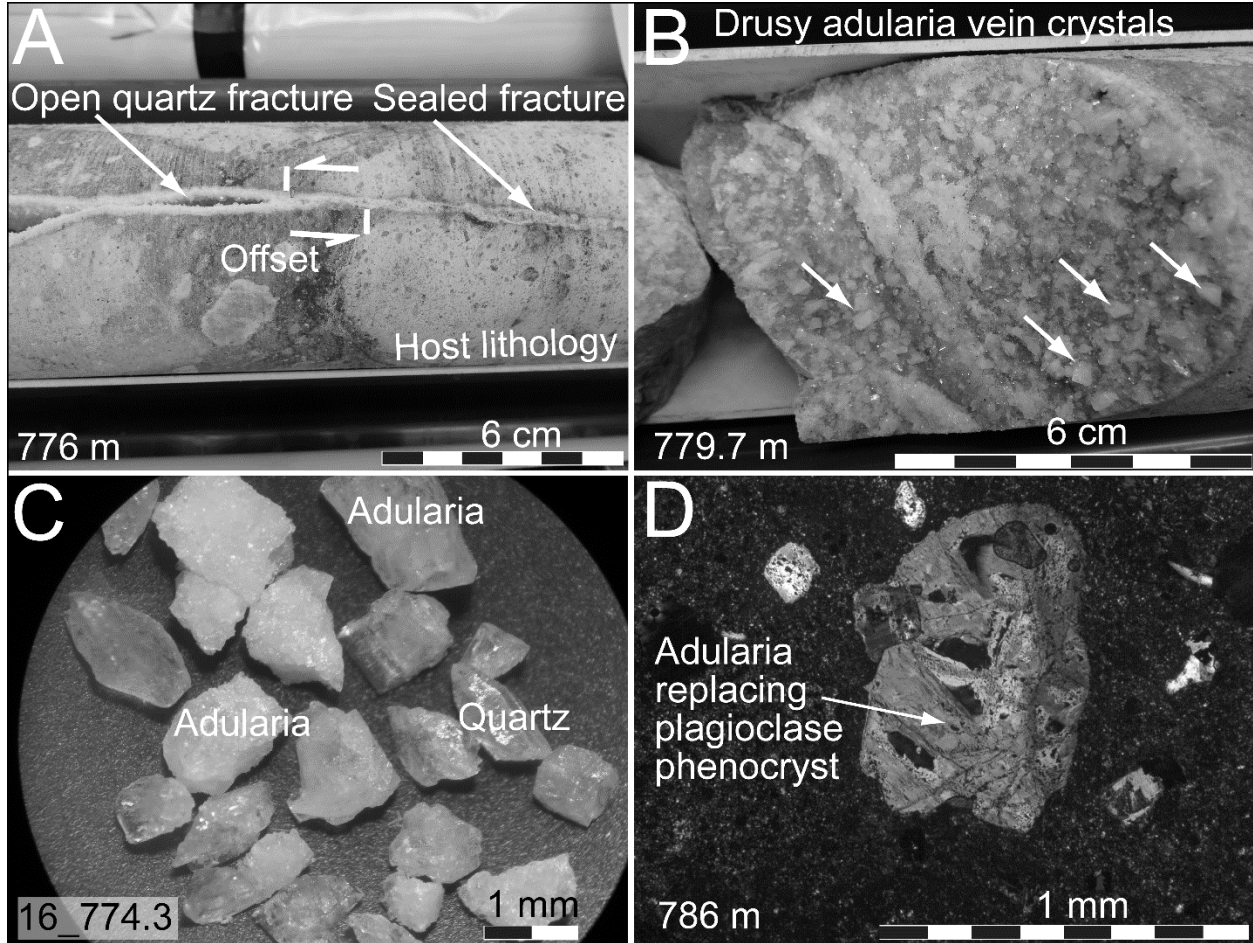


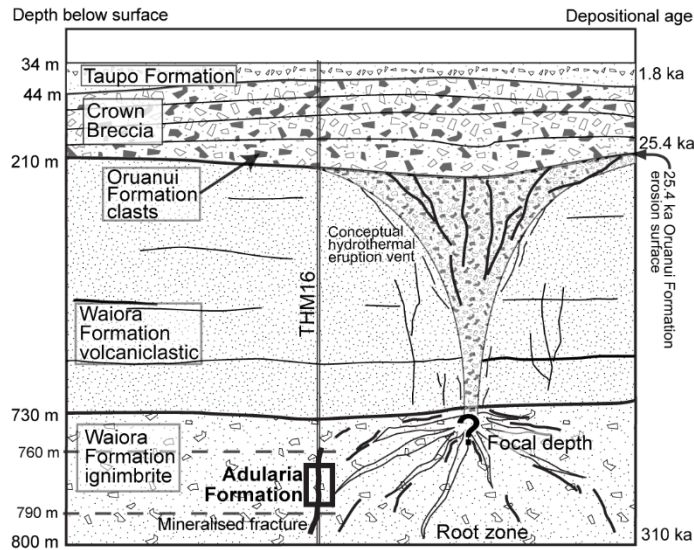
Supplementary Materials



**Supplemental Figure DR1.** A. Map showing the location of the Taupo Volcanic Zone (TVZ) and the offshore subduction setting at North Island, New Zealand. B. The geographical boundary of young TVZ (from Wilson et al., 1995) illustrating the distribution of the southern cone volcanoes (speckled), eight caldera centres (dashed lines), 25 geothermal systems (grey dots) and central Lake Taupo (light grey area). Box denotes location of Wairakei-Tauhara Geothermal Field (Wairakei-Tauhara). C. Geographic architecture of Wairakei-Tauhara defined by an electrical resistivity boundary and bisected by the Waikato River and Taupo Fault Belt (solid lines). Open circles are drilled wells and those described in the text are labeled. Inferred distribution of Crown Breccia is shown.



**Supplemental Figure DR2.** Photographs of the samples used. A. Section of drill core (6.3 cm diameter) intersecting an offset mineralized fracture with hydrothermal quartz in Waiora Formation ignimbrite host rock at 776 m depth. B. Cored fracture surface with drusy rhombic adularia highlighted (arrows) at 779.7 m collected for analysis. C. Adularia and quartz crystals under binocular microscope before handpicking separation of sample 16\_774.3. D. Thin section of host rock at 786 m under cross-polarised light at 10× magnification showing patchy feldspar pseudomorph and groundmass replaced by pervasive hydrothermal adularia and quartz, respectively.



**Supplemental Figure DR3.** Conceptual illustration of the post-25.4 ka Crow Breccia vent and the stratigraphy of well THM16 (Rosenberg et al., 2009). The proposed mechanism and interpreted location is shown for the < 30 ka mineralized fracture containing hydrothermal adularia.

### CO<sub>2</sub> Laser Fusion <sup>40</sup>Ar/<sup>39</sup>Ar Measurements

Ar measurements were single-crystal, CO<sub>2</sub> laser fusion analyses performed with a Nu Instruments Noblesse multicollecting mass spectrometer fitted with a high mass Faraday cup and two low mass ion-counting detectors (Coble et al., 2011). Process control software developed in LabVIEW<sup>®</sup> by Jeremy Hourigan (Santa Cruz Laser Microfurnace) manages the laser output, vision, and stage motion as well as gas purification and the vacuum system. The Noblesse mass spectrometer is digitally interfaced with the extraction line control system for unattended analysis over several days. The Noblesse acquires <sup>40</sup>Ar/<sup>39</sup>Ar analyses by dynamically selecting between one of two procedures at the time gas is inlet into the mass spectrometer. Signal size is continuously monitored on the Faraday detector as gas is inlet into the mass spectrometer over the 15 seconds required for equilibration for the extraction line to occur. Most gas aliquots are sufficiently large (e.g., > 1x10<sup>-15</sup> mol <sup>39</sup>Ar) to use a multi-collecting procedure that involves a peak hop between the mass station used to measure <sup>40</sup>Ar-<sup>38</sup>Ar-<sup>36</sup>Ar and that used to measure <sup>39</sup>Ar

and  $^{37}\text{Ar}$  (method 3 in Coble et al., 2011). Smaller gas aliquots are dynamically selected to be measured in monocollection mode using the axial ion counter. In either procedure, the first measurements are acquired within 20 seconds of inletting the sample gas. Both procedures collect 300 seconds of data per  $^{40}\text{Ar}/^{39}\text{Ar}$  analysis.

The overall approach for standardizing the  $^{40}\text{Ar}/^{39}\text{Ar}$  measurements is described in Coble et al. (2011). The measurement procedures employed in this study were standardized using a newly synthesized reference gas prepared in collaboration with Dr. Andrew Calvert at the U.S. Geological Survey (Menlo Park) that was put into service in June, 2015. In calculating  $^{40}\text{Ar}/^{39}\text{Ar}$  ages, we use a decay constant of  $\lambda = 5.543 \times 10^{-10}/\text{a}$  (Steiger and Jäger, 1977) that remains consistent with current best estimates (Renne et al., 2011). There is currently no consensus regarding the true  $^{40}\text{Ar}/^{40}\text{K}$  of ca. 28 Ma Fish Canyon sanidine (FCs) or any other flux monitor in use for  $^{40}\text{Ar}/^{39}\text{Ar}$  analysis. The range of K-Ar ages ascribed to FCs on the basis of different approaches define a spread of more than 1% (e.g., Phillips and Machan, 2013) and thus requires that the accuracy of  $^{40}\text{Ar}/^{39}\text{Ar}$  results must also be percent level at best. In this study, we have assigned Taylor Creek sanidine a K-Ar age of 28.34 Ma that corresponds to a K-Ar age of 28.02 Ma for FCs given R-values measured in the Stanford Noble Gas Laboratory (e.g., Renne et al., 1998). J-factor data calculated as outlined in McDougall and Harrison (1999). Inverse isochron model ages were calculated as described in Mahon (1996). We prefer inverse isochron ages to weighted mean of total gas ages because the adularia analyzed in this study indicated a “trapped”  $^{40}\text{Ar}/^{36}\text{Ar}$  ratios of 291 that is distinctly lower than the atmospheric value of 298.6 (Lee et al., 2006).

### **Laser Diode $^{40}\text{Ar}/^{39}\text{Ar}$ Incremental Heating**

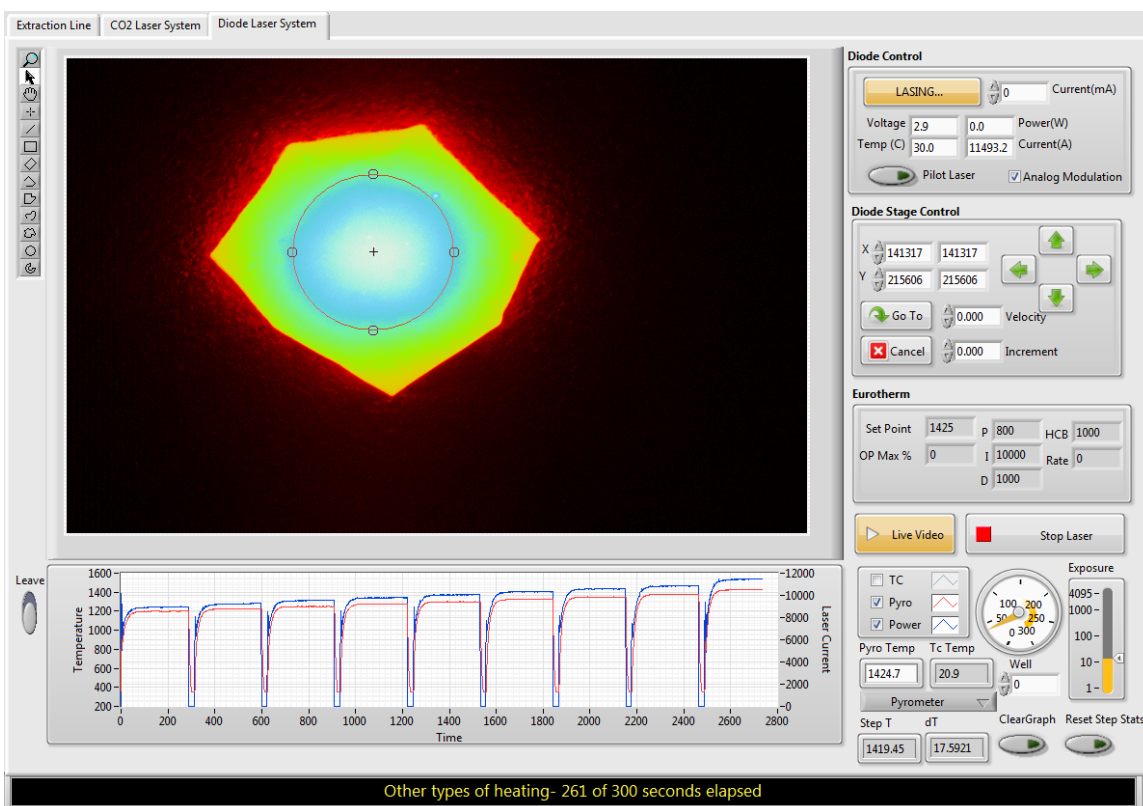
The same extraction line/mass spectrometer system was used as described above for  $\text{CO}_2$  laser fusion. A near-infrared ( $\lambda = 908$  nanometer), 75 watt Jenoptik® fiber optic diode laser with

beam delivery optics focused to a spot of ca. 2 mm supplied the radiation used to heat the sample. Tantalum is used to encapsulate the sample because Ta foil is refractory, malleable, and significantly absorbs 908 nanometer laser light.

To determine the Ar diffusion properties of the adularia examined in this study, a 1 mg sample was enclosed in a 3 mm disk of Ta foil. The encapsulation process is accomplished as follows. A single crystal or multiple crystals generally weighing a total of 0.05 to 2 milligrams are placed within a 3 mm diameter x 1 mm tall cylindrical base punched from a 5 mm diameter x 0.0025 thick disc of Ta foil. The crystals are covered with a 3 mm diameter disk of the same thickness. The packet is then folded about the sample (see Supplemental Fig. DR4 for typical final geometry). By virtue of its small total mass (< 2 milligrams sample + 10 milligrams of Ta foil), a laser heated microfurnace enables lower procedural blanks, more responsive temperature control, and lower experimental cost than is characteristic of a conventional resistance furnace fitted with refractory metal crucibles whose mass is on the order of a kilogram (McDougall and Harrison, 1999).

The Ta packet rests upon a stainless steel substrate within the diode laser chamber and is incrementally-heated via a laser through a sapphire window (Supplemental Fig. DR4). Continuous exposure of the evolved sample gas to a 50 l/s SAES st-707 getter pump maintains static vacuum to  $< 5 \times 10^{-7}$  Torr during heating. Non-contact temperature measurements were acquired with a 1.6  $\mu\text{m}$  spectral range optical pyrometer (Omega<sup>®</sup> OS1562 sensor) whose fiber optic focusing lenses ( $f = 125$  mm) sampled a 0.8 mm diameter region that was manually centered upon a heated target by adjusting the goniometer screws on its kinematic mount to maximize temperature. A CCD camera mated to a Navitar zoom microscope and fitted with an infrared

short pass cutoff wavelength filter imaged the  $< 850$  nanometer radiation generated by the heated sample.



**Supplemental Figure DR4.** Image of ca. 3 mm diameter Ta foil packet heated by diode laser to 1425°C. The CCD camera image of the  $< 850$  nanometer light emitted by the heated sample has been processed to reveal intensity gradients. The 2mm diameter of the green calibration guide shown in Figure DR-1 is 2 mm. The optical pyrometer samples the inner 0.8 mm of this region.

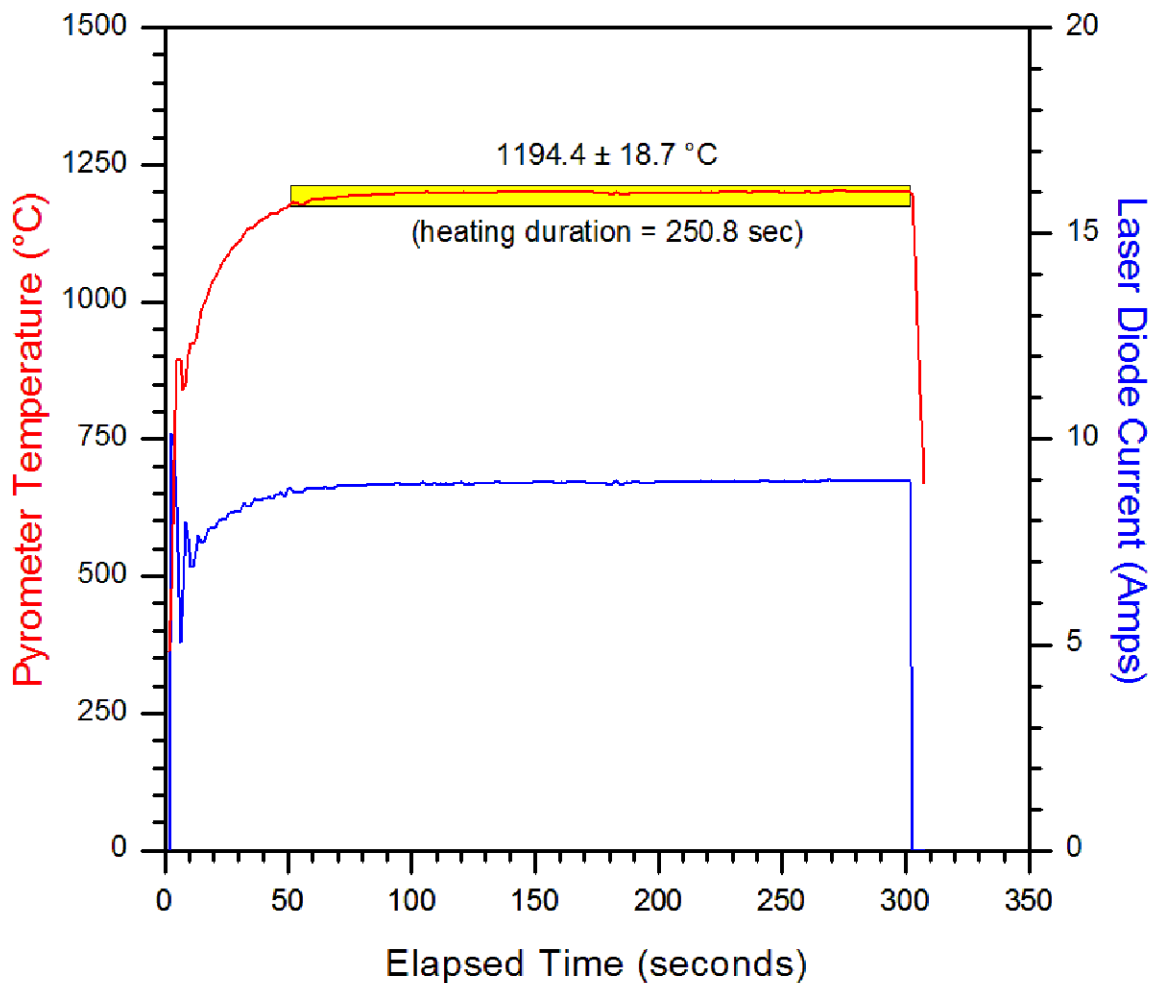
This output was processed to qualitatively represent temperature gradients at the sample surface (Supplemental Fig. DR4).

Although diode lasers are very responsive in heating the sample when used in current modulation mode, the temperature corresponding to a given current setting can only be approximately predicted and tends to decrease over the duration of the heating step due to diffusive heat loss to the much cooler metal substrate. Laser power was thus externally modulated to maintain constant sample temperature via a feedback loop established between the optical pyrometer signal, a Eurotherm® 2416 process controller, and the Ostech® laser

controller. Temperature was regulated using PID (proportional-integral-derivative) control algorithms in concert with maximum output power limits that were adjusted by the LabVIEW control software as a function of temperature.

In current modulation mode, peak temperature can be achieved in < 5 seconds of laser startup. However, external modulation based upon independent temperature measurement is required to achieve stable sample temperature. Tuning of the PID parameters and maximum power output limit was thus performed with the goal of preventing temperature overshoot rather than ensuring the most rapid attainment of set temperature. Avoiding temperature overshoot is important because diffusion is an exponential function of temperature. However, the negative consequence of dampening laser power to prevent overshoot at the onset of a heating step is that it produces a significant delay in the attainment of set temperature (Supplemental Fig. DR5).

To properly determine the heating duration in this situation, we first calculate a weighted mean temperature from the temperature-time data of the heating step. Each optical pyrometer temperature measurement in the time series (measured once per second) is normalized by a weighting factor,  $\exp[-A/T(K)]$ . We set  $A = 25000$  to correspond to an activation energy of ca. 50 kcal/mol which is typical of many silicates silicates. Weighted mean temperatures calculated in this manner are biased towards the higher temperatures that are the most important for facilitating diffusion. For example, temperatures of 500°C, 600°C, and 700°C are weighted by the factors  $9.0 \times 10^{-15}$ ,  $3.7 \times 10^{-13}$ , and  $6.9 \times 10^{-12}$ , respectively. Following this approach, the heating duration corresponds to the interval during which the temperature was within  $\pm 1$  standard error of the weighted mean) (Supplemental Fig. DR5).



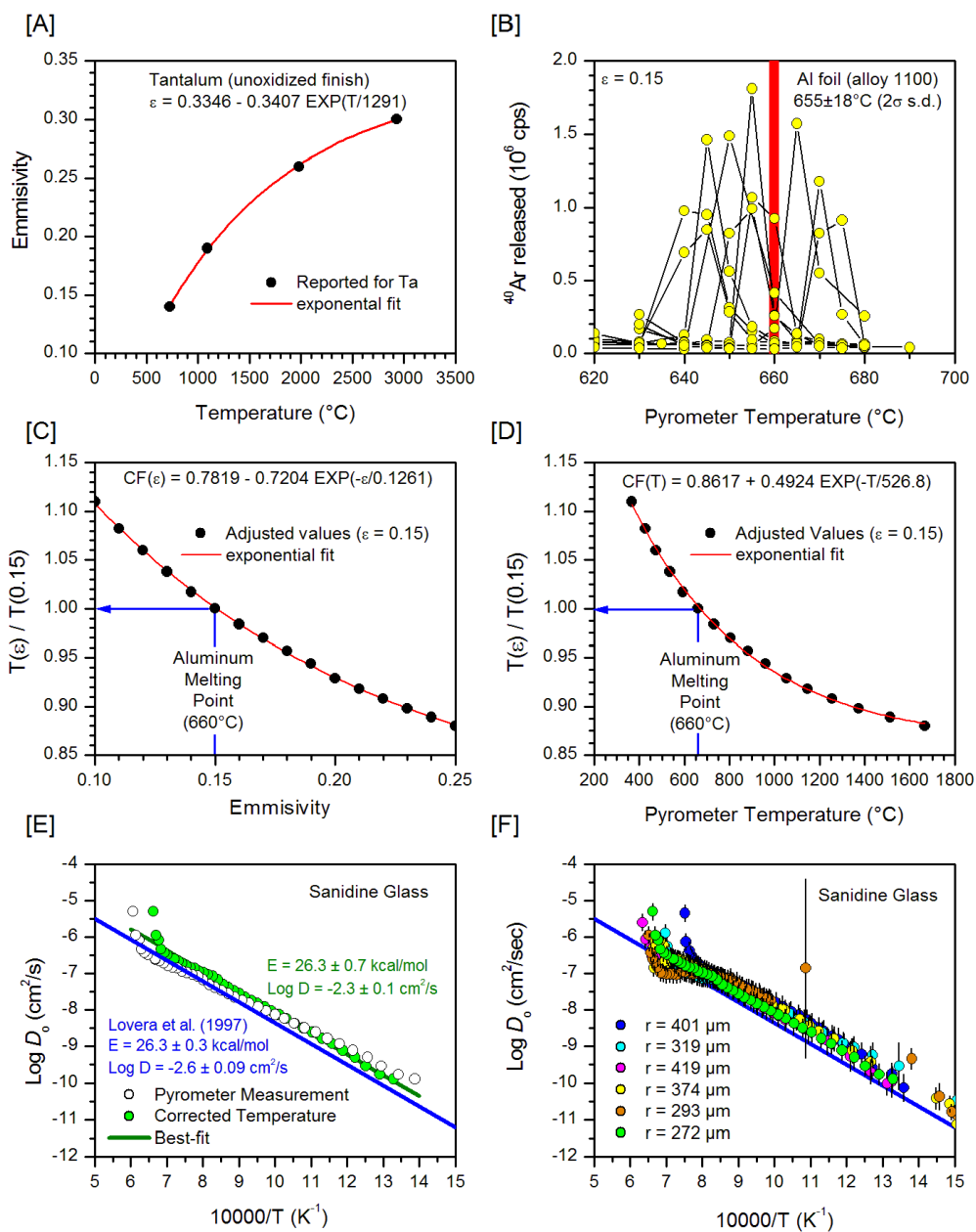
**Supplemental Figure DR5.** Illustration of method used to calculate the weighted mean temperature and duration of a heating step. Yellow box represents  $\pm 1$  s.e. of the weighted mean. The heating duration is calculated from the time that the temperature rises to within one standard error of the mean until the time that laser power is disabled.

All optical pyrometers must be calibrated to yield accurate temperature measurements. The temperature indicated by an optical pyrometer is a function of the emissivity of the target which in turn depends upon the target temperature and the wavelength of radiation monitored (Supplemental Fig. DR6A). The emissivity of Ta is a function of temperature, the oxidation state of its surface, and other environmental factors. The primary calibration of an optical pyrometer is made by measuring the infrared emission produced within a deep cavity formed within a heated metal object that approximates a black body source. Because this configuration differs

significantly from that of a reflective metal packet resting upon a colder metal substrate, the primary optical pyrometer calibration will be inaccurate.

Thermocouple calibration of optical pyrometer measurement is a widely used approach employed for many different types of experiments. In spite of the apparent simplicity of the approach, we have concluded that the method does not produce reliable data for our particular experimental setup, particularly at temperatures above 1100°C. The main difficulty is that even a very fine gauge thermocouple lead has equivalent or greater mass than the sample. For Ta-enclosed samples suspended upon a thermocouple, the heat conduction into the thermocouple leads thus requires significantly more laser power to heat the sample to a given temperature. At temperatures above 1100°C, differential thermal expansion of the thermocouple leads begins to produce instability as the position of the packet starts to shift relative to the centerlines of the laser beam and the optical pyrometer. The resulting temperature oscillation is a consequence of feedback between the temperature dependence of thermal expansion and the control loop between the fixed position optical pyrometer and the diode laser power controller. A final problem is that our need to heat  $^{40}\text{Ar}/^{39}\text{Ar}$  samples to 1500°C requires use of unwieldy and difficult to weld W-Rh thermocouple wire.

Our solution for calibration of the optical pyrometer avoids the above mentioned difficulties by performing experiments on reference materials of known thermal properties that are completely enclosed within our standard 3mm Ta foil packets. The procedures employed to calibrate the optical pyrometer are standard for  $^{40}\text{Ar}/^{39}\text{Ar}$  analysis. We perform two different types of calibration experiments: (1) melting of a disc of aluminum metal; and (2) incremental heating of sanidine glass.



**Supplemental Figure 6.** A. Emissivity of unoxidized tantalum reported in industry compilations (<http://www.omega.com/literature/transactions/volume1/emissivitya.html>). B. Melting point experiments performed with Al foil to calibrate emissivity of the pyrometer system at  $660^{\circ}\text{C}$ . C. Temperature dependence of the pyrometer temperature at constant laser power when emissivity is varied. D. Correction factor for temperature when pyrometer is operated at a constant emissivity ( $\epsilon = 0.15$  in this example). E. Diffusion data from sanidine glass (white circles) vs. those previously reported by Lovera et al. (1997) for resistance furnace measurements (blue line). Correction of the optical pyrometer temperatures results in green filled circles. Regression of these data reproduces the activation energy of Lovera et al. (1997). F. Reproducibility of laser diode diffusion results when temperature is measured with an optical pyrometer and corrected as discussed in the text.

### *Aluminum Melting Point*

Aluminum is used as a temperature calibration standard because its melting temperature is well known (660°C) and thus allows us to determine an emissivity value with a known temperature (Supplemental Fig. DR6A). An additional quality of manufactured aluminum is that large quantities of <sup>40</sup>Ar are present within Al foil because argon gas is bubbled through molten aluminum during the manufacturing process to rid it of hydrogen impurities that adversely affects its mechanical properties. Thus, melting of the Ta-encapsulated Al disk can be monitored by using the mass spectrometer to monitor release of <sup>40</sup>Ar as melting occurs (Supplemental Fig. DR6B).

In the Al melting experiments, a 3 mm diameter x 0.05 thick disk of alloy 1100 aluminum is fully enclosed within a standard Ta packet and incrementally heated through its melting point with the diode laser. Once the melting point has been detected, we correct the temperature reported by the optical pyrometer to a value of 660°C (i.e., the melting point of aluminum) by adjusting the pyrometer's emissivity setting. Replicate measurements of Ta-encapsulated Al foil indicate a temperature reproducibility of  $\pm 18$  °C ( $2\sigma$ ).

The emissivity determined in this calibration procedure yielded a value,  $\epsilon = 0.15$ , which nominally corresponds to a temperature of ca. 790°C (Supplemental Fig. DR6A). We attribute this 130°C temperature offset relative to the primary calibration of the optical pyrometer with a blackbody source in terms of a temperature gradient between the surface of the Ta foil packet and the interior of the packet (see also temperature gradients manifest in Supplemental Fig. DR4). Such high temperature gradients are supported by thermocouple measurements taken at the upper surface, within, and at the lower surface of the Ta packets.

### *Sanidine Glass Diffusion Properties*

The optical pyrometer used for the measurements reported in this paper was operated at a constant value of emissivity (set to 0.15 as discussed above). Pyrometer temperatures measured at this constant emissivity setting that are either above or below 660°C must be corrected. The correction requires knowledge of the temperature dependence of the pyrometer temperature reading as a function of the emissivity (Supplemental Fig. DR6A). We determine this function operationally by illuminating a Ta packet with at a constant power setting to ensure constant temperature at an emissivity of 0.15. Leaving laser power constant, we then measure the variation of the temperature reported by the optical pyrometer as the emissivity setting is systematically varied from 0.05 to 0.30 (Supplemental Fig. DR6C). From this data, it is simple to use the functional form of the relationship shown in Supplemental Fig. DR6A to map out a temperature dependent function that corrects fixed emissivity temperature measurements (see exponential relationship in Supplemental Fig. DR6D).

The validity of the optical pyrometer calibration (Supplemental Fig. DR6D) is confirmed by performing a step-heating sequence to generate diffusion data for a material whose Ar diffusion parameters have been measured using a thermocouple in a Ta crucible within a double vacuum resistance furnace (e.g., Lovera et al., 1997). To do this, we prepare near-spherical glass spheres of sanidine glass by air abrasion and enclose a single 300-400 micron radius sphere in a tantalum packet for each calibration run. The Arrhenius parameters of sanidine glass as measured in a resistance furnace are  $E = 26.3 \pm 0.3$  kcal/mol and  $D_0 = -2.6 \pm 0.09$  cm<sup>2</sup>/s (see Lovera et al., 1997). As expected from Supplemental Fig. DR6A, the nominal temperatures reported by the optical pyrometer with fixed emissivity ( $\epsilon = 0.15$ ) are progressively too low at temperatures below 660°C and too high at temperatures above this value. This error causes the slope of the

calculated diffusivities to be lower than the result obtained by resistance furnace heating using a thermocouple (Supplemental Fig. DR6E). Adjusting the optical pyrometer temperatures via the relationship shown in Figure Supplemental Fig. DR6D, yields the correct activation energy (see filled green circles in Supplemental Fig. DR6E). Supplemental Fig. DR6F demonstrates that this optical pyrometer calibration approach is reproducible for different packets measured in a time series of diffusion measurements performed over several weeks.

### Multi-Diffusion Domain Analysis of Adularia

The multi-diffusion domain (MDD) properties of adularia were calculated using a routine (Arrmulti.exe) presented in Lovera et al. (1997). The following domain distribution was employed in calculations used in our study ( $E = 45.1 \pm 2.4$  kcal/mol;  $\text{Log}D_o/r_o^2 = 3.1 \pm 0.5$  s<sup>-1</sup>):

Domain	Log $D_o/r_o^2$	$f_i$
1	5.35788	0.03671
2	2.76806	0.14044
3	2.73414	0.10071
4	2.68372	0.11855
5	2.52632	0.15157
6	2.43458	0.12433
7	2.07767	0.28794
8	1.90475	0.03975

Fractional loss calculations were performed using a routine (agesme.exe) described in Lovera et al. (1991). Temperature was initially set to 1000°C to outgas adularia. Then a constant temperature and heating duration was specified. The fractional loss (F) was calculated from the expression:  $F (\%) = 100 \times [1 - (\text{total gas age})/(\text{heating duration})]$ .

## References Cited

- Coble, M.A., Grove, M.J., and Calvert, A.T., 2011, Calibration of Nu-Instruments Noblesse multicollector mass spectrometers for argon isotopic measurements using a newly developed reference gas: *Chemical Geology*, v. 290, no. 1-2, p. 75–87.
- Lovera, O.M., 1992, Computer programs to model  $^{40}\text{Ar}/^{39}\text{Ar}$  diffusion data from multi-domain samples. *Computers and Geosciences* v.18, p.789-813.
- Lovera, O.M., Grove, M., Harrison, T.M., and Mahon, K.I., 1997, Systematic analysis of K-feldspar  $^{40}\text{Ar}/^{39}\text{Ar}$  step-heating experiments I: Significance of activation energy determinations. *Geochim. Cosmochim. Acta*, v.61, p.3171-3192.
- McDougall, I., and Harrison, T.M., 1999, *Geochronology and Thermochronology by the  $^{40}\text{Ar}/^{39}\text{Ar}$  Method*, 2nd ed.: New York, Oxford University Press, 269 p.
- McDougall, I., and Wellman, P., 2011, Calibration of GA1550 biotite standard for K-Ar and  $^{40}\text{Ar}/^{39}\text{Ar}$  dating: *Chemical Geology*, v. 280, p. 19–25.
- Miiller, A.P., 2006, Development of argon isotope reference standards for the U.S. Geological Survey: *Journal of Research of the National Institute of Standards and Technology*, v.111, p. 335-360.
- Phillips, D., and Matchan, E.L., 2013, Ultra-high precision  $^{40}\text{Ar}/^{39}\text{Ar}$  ages for Fish Canyon Tuff and Alder Creek Rhyolite sanidine: New dating standards required?: *Geochimica et Cosmochimica Acta*, v. 121, p. 229–239.
- Mahon, K.I., 1996, The New “York” regression: Application of an improved statistical method to geochemistry: *International Geology Review*, v. 38, no. 4, p. 293-303.
- Renne, P.R., Balco, G., Ludwig, K.R., Mundil, R., and Min, K., 2011, Response to the comment by W.H. Schwarz et al. on “Joint determination of  $^{40}\text{K}$  decay constants and  $^{40}\text{Ar}^*/^{40}\text{K}$  for

- the Fish Canyon sanidine standard, and improved accuracy for  $^{40}\text{Ar}/^{39}\text{Ar}$  geochronology”  
by P.R. Renne et al. (2010): *Geochimica et Cosmochimica Acta*, v. 75, p. 5097–5100.
- Rosenberg, M., Ramirez, L., Kilgour, G., Milicich, S., and Manville, V., 2009, Tauhara  
subsidence investigation project: geological summary of Tauhara Wells THM12-18 and  
THM21-22 and Wairakei Wells WKM14-15: GNS Science Consultancy Report, v. 2009,  
p. 52.
- Steiger, R.H., and Jäger, E., 1977, Subcommittee on geochronology: convention on the use of  
decay constants in geo- and cosmochronology: *Earth and Planetary Science Letters*, v.36,  
p. 359–362.
- Wilson, C., Houghton, B., McWilliams, M., Lanphere, M., Weaver, S., and Briggs, R., 1995,  
Volcanic and structural evolution of Taupo Volcanic Zone, New Zealand: a review:  
*Journal of Volcanology and Geothermal Research*, v. 68, p. 1-28.

Sample 1OZE (ADULARIA) Single Crystal CO<sub>2</sub> Laser Fusion (J = 1.920E-03)

Step	<sup>40</sup> Ar/ <sup>39</sup> Ar <sup>1</sup>	<sup>38</sup> Ar/ <sup>39</sup> Ar <sup>1</sup>	<sup>37</sup> Ar/ <sup>39</sup> Ar <sup>1</sup>	<sup>36</sup> Ar/ <sup>39</sup> Ar <sup>1</sup>	<sup>39</sup> Ar (mol) <sup>2</sup>	<sup>40</sup> Ar*/ <sup>39</sup> Ar <sup>3</sup>	± 1 s.d.	<sup>39</sup> Ar/ <sup>40</sup> Ar	± 1 s.d.	<sup>36</sup> Ar/ <sup>40</sup> Ar	± 1 s.d.	Age (Ma) <sup>3</sup>	± 1 s.d.
1	0.24859	1.29E-02	1.33E-04	8.20E-04	2.04E-14	1.44E-03	3.03E-03	4.104	0.018	3.364E-03	4.206E-05	4.98E-03	1.05E-02
2	0.47143	1.31E-02	1.57E-04	1.60E-03	2.07E-14	-5.58E-03	4.03E-03	2.144	0.008	3.425E-03	2.929E-05	-1.93E-02	1.40E-02
3	0.45634	1.30E-02	3.13E-04	1.53E-03	1.84E-14	-8.70E-04	3.40E-03	2.215	0.007	3.391E-03	2.549E-05	-3.02E-03	1.18E-02
4	0.31568	1.28E-02	1.46E-04	1.05E-03	2.32E-14	1.22E-03	2.94E-03	3.218	0.011	3.371E-03	3.201E-05	4.22E-03	1.02E-02
5	0.96147	1.33E-02	1.45E-04	3.24E-03	2.55E-14	-3.64E-04	6.28E-03	1.045	0.003	3.385E-03	2.222E-05	-1.26E-03	2.18E-02
6	0.15837	1.28E-02	1.33E-04	5.07E-04	1.79E-14	3.61E-03	3.69E-03	6.517	0.112	3.304E-03	8.036E-05	1.25E-02	1.28E-02
7	0.21383	1.28E-02	1.35E-04	6.89E-04	1.95E-14	5.31E-03	2.61E-03	4.787	0.024	3.298E-03	4.217E-05	1.84E-02	9.06E-03
8	0.27457	1.29E-02	1.44E-04	9.29E-04	2.09E-14	-5.00E-03	2.97E-03	3.709	0.016	3.447E-03	3.744E-05	-1.73E-02	1.03E-02
9	0.31623	1.29E-02	1.06E-04	1.08E-03	1.15E-14	-8.51E-03	4.32E-03	3.212	0.014	3.477E-03	4.713E-05	-2.95E-02	1.50E-02
10	0.61631	1.32E-02	1.51E-04	2.11E-03	8.38E-15	-1.28E-02	7.15E-03	1.636	0.008	3.455E-03	3.973E-05	-4.42E-02	2.48E-02
11	0.19390	1.28E-02	1.44E-04	6.33E-04	1.04E-14	1.96E-03	4.05E-03	5.292	0.049	3.349E-03	7.246E-05	6.79E-03	1.40E-02
12	0.36611	1.30E-02	1.39E-04	1.21E-03	1.65E-14	3.26E-03	3.65E-03	2.769	0.009	3.354E-03	3.416E-05	1.13E-02	1.26E-02
13	0.12788	1.27E-02	1.18E-04	4.02E-04	1.92E-14	4.23E-03	2.43E-03	8.134	0.061	3.268E-03	6.653E-05	1.46E-02	8.41E-03
14	0.17829	1.28E-02	1.07E-04	5.79E-04	2.13E-14	2.40E-03	2.72E-03	5.769	0.041	3.337E-03	5.286E-05	8.32E-03	9.41E-03
15	0.09869	1.27E-02	1.16E-04	3.13E-04	1.56E-14	1.39E-03	2.66E-03	10.67	0.13	3.334E-03	9.577E-05	4.82E-03	9.22E-03
16	0.22229	1.28E-02	1.31E-04	7.29E-04	1.23E-14	1.98E-03	3.55E-03	4.601	0.035	3.353E-03	5.522E-05	6.84E-03	1.23E-02
17	0.27482	1.29E-02	1.12E-04	9.09E-04	1.88E-14	1.33E-03	3.31E-03	3.705	0.022	3.367E-03	4.146E-05	4.61E-03	1.15E-02
18	0.16359	1.27E-02	9.83E-05	5.29E-04	1.51E-14	2.43E-03	3.13E-03	6.303	0.076	3.332E-03	6.638E-05	8.42E-03	1.08E-02
19	0.15753	1.27E-02	1.07E-04	5.07E-04	1.16E-14	2.88E-03	3.57E-03	6.553	0.056	3.320E-03	7.900E-05	9.98E-03	1.24E-02

Sample 2OZE (ADULARIA) Single Crystal CO<sub>2</sub> Laser Fusion (J = 1.920E-03)

Step	<sup>40</sup> Ar/ <sup>39</sup> Ar <sup>1</sup>	<sup>38</sup> Ar/ <sup>39</sup> Ar <sup>1</sup>	<sup>37</sup> Ar/ <sup>39</sup> Ar <sup>1</sup>	<sup>36</sup> Ar/ <sup>39</sup> Ar <sup>1</sup>	<sup>39</sup> Ar (mol) <sup>2</sup>	<sup>40</sup> Ar*/ <sup>39</sup> Ar <sup>3</sup>	± 1 s.d.	<sup>39</sup> Ar/ <sup>40</sup> Ar	± 1 s.d.	<sup>36</sup> Ar/ <sup>40</sup> Ar	± 1 s.d.	Age (Ma) <sup>3</sup>	± 1 s.d.
1	0.5126	1.31E-02	-3.35E-05	1.80E-03	2.78E-15	-2.29E-02	2.02E-02	1.970	0.055	3.536E-03	1.378E-04	-7.92E-02	7.00E-02
2	0.3447	1.29E-02	1.52E-04	1.16E-03	7.04E-15	-1.87E-03	6.97E-03	2.944	0.040	3.403E-03	6.963E-05	-6.47E-03	2.42E-02
3	0.0819	1.28E-02	9.42E-05	2.49E-04	2.31E-14	3.41E-03	1.88E-03	12.99	0.12	3.234E-03	8.225E-05	1.18E-02	6.53E-03
4	0.2763	1.29E-02	1.38E-04	9.05E-04	3.17E-15	3.89E-03	1.23E-02	3.685	0.068	3.336E-03	1.526E-04	1.35E-02	4.25E-02
5	0.1335	1.28E-02	1.23E-04	4.60E-04	3.57E-15	-7.48E-03	8.69E-03	7.780	0.255	3.581E-03	2.319E-04	-2.59E-02	3.01E-02
6	0.6501	1.31E-02	1.99E-04	2.24E-03	4.81E-15	-1.72E-02	1.08E-02	1.550	0.010	3.474E-03	5.681E-05	-5.95E-02	3.74E-02
7	0.2327	1.28E-02	9.51E-05	7.65E-04	1.13E-14	1.64E-03	5.14E-03	4.390	0.053	3.360E-03	7.621E-05	5.69E-03	1.78E-02
8	0.5168	1.30E-02	1.38E-04	1.75E-03	9.57E-15	-4.24E-03	4.83E-03	1.954	0.007	3.412E-03	3.199E-05	-1.47E-02	1.67E-02
9	0.3783	1.30E-02	1.08E-04	1.24E-03	3.78E-15	6.08E-03	1.03E-02	2.678	0.044	3.329E-03	9.290E-05	2.11E-02	3.57E-02
10	0.0759	1.27E-02	7.76E-05	2.12E-04	3.77E-15	8.47E-03	8.45E-03	14.08	0.99	2.980E-03	3.869E-04	2.93E-02	2.93E-02
11	0.1049	1.27E-02	1.23E-04	3.31E-04	1.57E-14	2.27E-03	2.85E-03	10.00	0.18	3.307E-03	9.559E-05	7.87E-03	9.87E-03
12	0.4094	1.32E-02	2.36E-04	1.34E-03	3.92E-15	8.44E-03	1.00E-02	2.472	0.034	3.313E-03	8.348E-05	2.92E-02	3.48E-02
13	0.1915	1.28E-02	1.23E-04	6.35E-04	7.28E-15	-1.09E-03	5.82E-03	5.362	0.109	3.404E-03	1.058E-04	-3.77E-03	2.02E-02
14	0.1877	1.28E-02	1.58E-04	6.24E-04	6.26E-15	-1.71E-03	6.22E-03	5.470	0.083	3.416E-03	1.153E-04	-5.93E-03	2.15E-02
15	0.6781	1.32E-02	1.94E-04	2.24E-03	4.49E-15	1.11E-02	1.09E-02	1.486	0.011	3.328E-03	5.483E-05	3.84E-02	3.79E-02
16	0.1256	1.28E-02	1.58E-04	3.96E-04	9.44E-15	3.65E-03	4.33E-03	8.288	0.137	3.282E-03	1.206E-04	1.26E-02	1.50E-02
17	0.0584	1.27E-02	1.20E-04	1.84E-04	1.03E-14	-8.33E-04	3.96E-03	18.69	0.89	3.437E-03	2.520E-04	-2.89E-03	1.37E-02
18	0.2682	1.29E-02	1.46E-04	9.00E-04	1.91E-14	-2.59E-03	3.13E-03	3.799	0.016	3.417E-03	4.032E-05	-8.95E-03	1.08E-02
19	0.2472	1.27E-02	1.21E-04	8.05E-04	1.13E-14	4.50E-03	3.79E-03	4.128	0.035	3.321E-03	5.259E-05	1.56E-02	1.31E-02
20	0.1275	1.28E-02	8.80E-05	4.05E-04	6.89E-15	2.90E-03	5.29E-03	8.158	0.210	3.304E-03	1.448E-04	1.01E-02	1.83E-02
21	0.5873	1.32E-02	9.43E-05	2.04E-03	8.85E-15	-1.96E-02	6.36E-03	1.717	0.006	3.498E-03	3.705E-05	-6.80E-02	2.20E-02
22	0.1869	1.28E-02	1.32E-04	5.91E-04	6.45E-15	7.36E-03	5.56E-03	5.495	0.068	3.247E-03	1.026E-04	2.55E-02	1.92E-02

Sample 3OZE (ADULARIA) Single Crystal CO2 Laser Fusion (J = 1.921E-03)

Step	$^{40}\text{Ar}/^{39}\text{Ar}^1$	$^{38}\text{Ar}/^{39}\text{Ar}^1$	$^{37}\text{Ar}/^{39}\text{Ar}^1$	$^{36}\text{Ar}/^{39}\text{Ar}^1$	$^{39}\text{Ar}(\text{mol})^2$	$^{40}\text{Ar}^*/^{39}\text{Ar}^3$	$\pm 1 \text{ s.d.}$	$^{39}\text{Ar}/^{40}\text{Ar}$	$\pm 1 \text{ s.d.}$	$^{36}\text{Ar}/^{40}\text{Ar}$	$\pm 1 \text{ s.d.}$	Age (Ma) <sup>3</sup>	$\pm 1 \text{ s.d.}$
1	1.3498	1.35E-02	2.24E-04	4.65E-03	2.72E-15	-3.00E-02	1.68E-02	0.744	0.003	3.460E-03	4.237E-05	-1.04E-01	5.82E-02
2	0.2311	1.28E-02	1.56E-04	7.71E-04	1.01E-14	-1.54E-03	4.49E-03	4.422	0.034	3.407E-03	6.720E-05	-5.33E-03	1.55E-02
3	0.2972	1.28E-02	1.62E-04	9.87E-04	5.73E-15	6.37E-04	9.17E-03	3.422	0.060	3.377E-03	1.061E-04	2.21E-03	3.18E-02
4	0.1694	1.29E-02	1.61E-04	5.60E-04	9.24E-15	-9.38E-04	4.53E-03	6.079	0.082	3.403E-03	9.335E-05	-3.25E-03	1.57E-02
5	0.1045	1.28E-02	1.78E-04	3.45E-04	1.26E-14	-2.25E-03	3.75E-03	10.05	0.26	3.461E-03	1.289E-04	-7.80E-03	1.30E-02
6	0.1039	1.27E-02	1.14E-04	3.27E-04	1.33E-14	2.18E-03	2.97E-03	10.11	0.12	3.309E-03	1.011E-04	7.56E-03	1.03E-02
7	0.1366	1.29E-02	1.04E-04	4.62E-04	1.72E-14	-4.76E-03	3.81E-03	7.597	0.179	3.506E-03	1.003E-04	-1.65E-02	1.32E-02
8	0.5182	1.32E-02	1.00E-04	1.77E-03	1.59E-14	-9.57E-03	4.72E-03	1.948	0.007	3.447E-03	3.118E-05	-3.32E-02	1.63E-02
9	0.2996	1.29E-02	9.93E-05	1.01E-03	1.75E-14	-4.83E-03	3.61E-03	3.393	0.016	3.440E-03	4.159E-05	-1.67E-02	1.25E-02
10	0.1750	1.28E-02	1.28E-04	5.68E-04	2.75E-14	2.33E-03	1.93E-03	5.879	0.029	3.338E-03	3.822E-05	8.09E-03	6.67E-03
11	0.1268	1.28E-02	1.25E-04	4.10E-04	2.42E-14	5.72E-04	1.81E-03	8.209	0.055	3.368E-03	5.013E-05	1.98E-03	6.26E-03
12	0.4067	1.31E-02	1.76E-04	1.37E-03	6.03E-15	-2.73E-03	7.82E-03	2.489	0.018	3.407E-03	6.589E-05	-9.47E-03	2.71E-02
13	1.0581	1.36E-02	1.79E-04	3.64E-03	6.89E-15	-2.20E-02	8.72E-03	0.950	0.002	3.455E-03	2.808E-05	-7.63E-02	3.02E-02
14	0.1528	1.29E-02	2.30E-04	5.04E-04	3.63E-15	-1.11E-03	9.55E-03	6.765	0.201	3.410E-03	2.190E-04	-3.86E-03	3.31E-02
15	0.3873	1.30E-02	1.38E-04	1.30E-03	8.37E-15	-2.84E-03	6.79E-03	2.615	0.023	3.409E-03	6.017E-05	-9.83E-03	2.35E-02
16	0.0947	1.27E-02	1.66E-04	2.85E-04	5.81E-15	5.49E-03	5.37E-03	11.14	0.43	3.177E-03	1.972E-04	1.90E-02	1.86E-02
17	0.5471	1.31E-02	2.23E-04	1.84E-03	8.17E-15	-1.80E-03	6.29E-03	1.844	0.008	3.395E-03	3.926E-05	-6.23E-03	2.18E-02
18	0.2080	1.27E-02	1.54E-04	6.78E-04	1.31E-14	2.66E-03	3.85E-03	4.926	0.057	3.340E-03	6.380E-05	9.22E-03	1.33E-02
19	0.2998	1.28E-02	1.38E-04	1.01E-03	2.00E-14	-4.70E-03	3.49E-03	3.391	0.016	3.438E-03	4.015E-05	-1.63E-02	1.21E-02
20	0.0772	1.27E-02	1.35E-04	2.42E-04	1.47E-14	6.56E-04	2.63E-03	13.84	0.25	3.353E-03	1.231E-04	2.27E-03	9.13E-03
21	0.0845	1.27E-02	2.07E-04	2.25E-04	5.66E-15	1.31E-02	5.55E-03	12.57	0.53	2.825E-03	2.227E-04	4.55E-02	1.92E-02
22	0.0999	1.27E-02	1.05E-04	2.97E-04	1.40E-14	7.15E-03	2.57E-03	10.53	0.13	3.129E-03	9.038E-05	2.48E-02	8.92E-03

Sample 4OZE (ADULARIA) Single Crystal CO2 Laser Fusion (J = 1.921E-03)

Step	$^{40}\text{Ar}/^{39}\text{Ar}^1$	$^{38}\text{Ar}/^{39}\text{Ar}^1$	$^{37}\text{Ar}/^{39}\text{Ar}^1$	$^{36}\text{Ar}/^{39}\text{Ar}^1$	$^{39}\text{Ar}(\text{mol})^2$	$^{40}\text{Ar}^*/^{39}\text{Ar}^3$	$\pm 1 \text{ s.d.}$	$^{39}\text{Ar}/^{40}\text{Ar}$	$\pm 1 \text{ s.d.}$	$^{36}\text{Ar}/^{40}\text{Ar}$	$\pm 1 \text{ s.d.}$	Age (Ma) <sup>3</sup>	$\pm 1 \text{ s.d.}$
1	1.0879	1.35E-02	2.13E-04	3.69E-03	4.08E-15	-6.52E-03	1.59E-02	0.923	0.010	3.404E-03	4.986E-05	-2.26E-02	5.51E-02
2	1.8643	1.40E-02	1.81E-04	6.27E-03	4.04E-15	6.88E-03	1.80E-02	0.538	0.003	3.372E-03	3.268E-05	2.38E-02	6.23E-02
3	0.1651	1.27E-02	1.43E-04	5.22E-04	1.20E-14	5.96E-03	5.19E-03	6.243	0.158	3.258E-03	1.071E-04	2.06E-02	1.80E-02
4	0.3190	1.29E-02	2.43E-04	1.03E-03	7.11E-15	8.85E-03	7.05E-03	3.184	0.048	3.289E-03	7.498E-05	3.07E-02	2.44E-02
5	0.2255	1.29E-02	1.92E-04	7.35E-04	8.80E-15	3.34E-03	4.84E-03	4.533	0.058	3.333E-03	7.385E-05	1.16E-02	1.68E-02
6	0.4664	1.31E-02	8.60E-06	1.54E-03	3.48E-15	7.20E-03	1.27E-02	2.167	0.035	3.331E-03	9.297E-05	2.49E-02	4.42E-02
7	0.1986	1.28E-02	1.34E-04	6.38E-04	1.41E-14	4.98E-03	3.76E-03	5.165	0.048	3.297E-03	6.542E-05	1.73E-02	1.30E-02
8	0.3623	1.29E-02	1.49E-04	1.19E-03	2.14E-14	4.32E-03	3.85E-03	2.798	0.015	3.343E-03	3.638E-05	1.50E-02	1.34E-02
9	0.1705	1.28E-02	1.53E-04	5.19E-04	9.05E-15	1.21E-02	5.28E-03	6.039	0.096	3.137E-03	1.061E-04	4.20E-02	1.83E-02
10	0.3389	1.29E-02	1.44E-04	1.12E-03	1.13E-14	1.66E-03	4.52E-03	2.994	0.018	3.367E-03	4.580E-05	5.74E-03	1.57E-02
11	0.1528	1.28E-02	1.48E-04	4.84E-04	1.68E-14	4.87E-03	3.09E-03	6.763	0.066	3.273E-03	7.026E-05	1.69E-02	1.07E-02
13	0.7893	1.32E-02	1.23E-04	2.63E-03	6.67E-15	7.87E-03	8.27E-03	1.275	0.006	3.350E-03	3.560E-05	2.73E-02	2.87E-02
14	0.2591	1.29E-02	1.77E-04	8.52E-04	1.24E-14	2.40E-03	3.96E-03	3.935	0.029	3.352E-03	5.268E-05	8.33E-03	1.37E-02
15	0.2229	1.28E-02	1.12E-04	6.81E-04	3.18E-15	1.66E-02	1.20E-02	4.589	0.148	3.126E-03	1.820E-04	5.77E-02	4.17E-02
16	0.6759	1.32E-02	5.96E-04	2.30E-03	5.06E-15	-7.27E-03	1.02E-02	1.490	0.011	3.421E-03	5.151E-05	-2.52E-02	3.53E-02
17	0.3068	1.29E-02	1.87E-04	1.04E-03	1.92E-14	-5.51E-03	3.37E-03	3.313	0.016	3.446E-03	3.794E-05	-1.91E-02	1.17E-02
18	0.3053	1.29E-02	1.27E-04	1.03E-03	1.76E-14	-4.84E-03	3.53E-03	3.330	0.025	3.439E-03	4.006E-05	-1.68E-02	1.22E-02
19	0.1294	1.28E-02	1.91E-04	4.03E-04	9.89E-15	5.46E-03	4.59E-03	8.035	0.162	3.236E-03	1.232E-04	1.89E-02	1.59E-02
20	0.7931	1.32E-02	1.43E-04	2.68E-03	2.22E-14	-4.67E-03	5.36E-03	1.269	0.004	3.404E-03	2.302E-05	-1.62E-02	1.86E-02
21	0.1449	1.28E-02	1.60E-04	4.78E-04	2.24E-14	-1.27E-03	2.52E-03	7.143	0.081	3.415E-03	6.119E-05	-4.41E-03	8.74E-03
22	0.1680	1.29E-02	1.29E-04	5.45E-04	3.41E-14	2.14E-03	2.01E-03	6.132	0.036	3.340E-03	4.158E-05	7.43E-03	6.97E-03

<sup>1</sup>Raw data corrected for ion counter deadtime; instrumental mass fractionation; procedural line blank; & radioactive decay of <sup>37</sup>Ar <sup>39</sup>Ar & <sup>36</sup>Cl

<sup>2</sup>Total <sup>39</sup>Ar normalized to 100% delivery to the Mass Spectrometer

<sup>3</sup>Corrected for nuclear interferences & trapped Ar (40Ar/36Ar = 298.5)

Flux Monitor: Taylor Creek Sanidine (28.34 Ma)

<sup>40</sup>Ar/<sup>39</sup>Ar<sub>K</sub>: 4.937E-03 ± 1.623E-03

<sup>38</sup>Ar/<sup>39</sup>Ar<sub>K</sub>: 4.937E-03 ± 1.623E-03

<sup>36</sup>Ar/<sup>37</sup>Ar<sub>Ca</sub>: 2.789E-04 ± 6.012E-06

<sup>39</sup>Ar/<sup>37</sup>Ar<sub>Ca</sub>: 2.789E-04 ± 6.012E-06

Analytical errors (±1 s.d.) only. Systematic errors associated with radioactive decay or irradiation correction factors are not propagated